ARCHIVIO ISTITUZIONALE DELLA RICERCA

Alma Mater Studiorum Università di Bologna
Archivio istituzionale della ricerca

Seismic surface wave attenuation by resonant metasurfaces on stratified soil

This is the final peer-reviewed author's accepted manuscript (postprint) of the following publication:

Published Version:
Zeng, C., Zhao, C., Zeighami, F. (2022). Seismic surface wave attenuation by resonant metasurfaces on stratified soil. EARTHQUAKE ENGINEERING & STRUCTURAL DYNAMICS, 51(5), 1201-1223 [10.1002/eqe.3611].

Availability:
This version is available at: https://hdl.handle.net/11585/857268 since: 2024-07-03

Published:
DOI: http://doi.org/10.1002/eqe.3611

Terms of use:

Some rights reserved. The terms and conditions for the reuse of this version of the manuscript are specified in the publishing policy. For all terms of use and more information see the publisher's website.

This item was downloaded from IRIS Università di Bologna (https://cris.unibo.it/).
When citing, please refer to the published version.

(Article begins on next page)

11 October 2026

SEISMIC SURFACE WAVE ATTENUATION BY RESONANT METASURFACES ON STRATIFIED SOIL

Chao Zeng[1], Chunfeng Zhao[1] and Farhad Zeighami[2]

[1]School of Civil Engineering, Hefei University of Technology, Hefei 230009, China

[2]Department of Civil, Chemical, Environmental and Materials Engineering - DICAM, University of Bologna, Bologna 40136, Italy

Correspondence

Chunfeng Zhao, School of Civil Engineering, Hefei University of Technology, Hefei, Anhui, 230009, China

E-mail: zhaowindy@hfut.edu.cn

Abstract

This study aims to theoretically and numerically investigate the dispersion relations of Rayleigh waves propagating through vertical oscillators periodically distributed on stratified media. The classical elastodynamics theory and an effective medium approximation method are adopted to describe the dynamic behavior of metasurfaces and hybridization between the local oscillators and the foundational surface wave modes. The Abo-zena algorithm and delta-matrix method are combined to simplify the eigen equation to overcome the accuracy problem in solving the closed-form dispersion laws and improve the computational efficiency. Subsequently, plane-strain finite element (FE) models with three configurations are developed to confirm the analytical predictions and obtain further insight into the resonator-Rayleigh wave coupling mechanism. The numerical results are in good agreement with the analytical solutions, revealing that only the foundational mode is strongly coupled with the vertical resonators at resonance, while the surface wave band gap reported in homogeneous media is crossed by the remaining higher-order surface modes. The attenuation performance and mechanical behavior of a finite-length metasurface are investigated, and it is demonstrated that the output surface ground motion can be significantly reduced in a narrow frequency band near resonance. Moreover, a graded resonant metasurface with decreasing frequency is simulated to assess the feasibility of broadband attenuation. In summary, the aforementioned analytical framework and numerical simulation results show that the vertical oscillators placed atop a stratified soil system can be designed as resonant metasurfaces for shielding seismic surface waves to protect multiple large infrastructures or special structures from earthquake hazards.

KEYWORDS

Resonant metasurfaces, Rayleigh waves, stratified soils, soil–resonator interaction, dispersion analysis, ground vibration attenuation

1 INTRODUCTION

Synthetic periodic structures with periodic unit cells or local resonant inclusions, namely, phononic crystals and elastic metamaterials, have been extensively studied to manipulate the propagation of acoustic and mechanical waves at different scales, resulting in frequency band gaps wherein wave propagation is suppressed.[1] Therefore, the

engineered periodic structures are expected to be applied for wave filtering and waveguiding through approaches that cannot be adopted in natural materials. In particular, the use of finite periodic structures to form elastic metamaterials can generate exceptional effects, including dispersion properties,[2–5] negative refraction,[6,7] and acoustic invisibility.[8,9] These effects have been widely used in optics, acoustics, and elastic media at both microscale and geophysical scales, such as superlensing,[10,11] wave guiding,[12–14] acoustic cloaking,[15–17] elastic wave obstacles,[18–20] and seismic wave mitigation.[20–24]

In 1987, Yablonovitch[2] and John[3] first reported the discovery of band gaps in their study of the propagation of light waves in periodic media. By introducing the concept of transformation optics in 2006, Leonhardt[25] and Pendry et al.[26] popularized the technique, based on which metamaterials control wave propagation. This concept has been applied at different geometric scales, ranging from nanometer-scale for thermal insulation[27] to meter-scale for seismic wave isolation.[20–24] For this reason, in the past two decades, many researchers have developed a variety of novel passive isolation devices utilizing periodicity and local resonances in civil engineering. Cheng and Shi[28] innovatively constructed a new type of seismic isolation device called periodic foundation, where inclusions are periodically embedded in matrix materials. Subsequently, Xiang[29] and Zhao et al.[23,24] experimentally and numerically analyzed the feasibility of a one-dimensional layered periodic foundation to attenuate longitudinal and shear waves in the 0–50 Hz frequency range. The results revealed that both the horizontal and vertical dynamic responses of the superstructure decreased noticeably when the excitation frequencies were within the band gaps. Considering that the surface wave components in seismic excitation are more harmful to infrastructures, Brûlé et al.[22] conducted a large-scale experiment in which a meter-sized periodic array of cylindrical holes was used to shield seismic surface waves, thereby mitigating ground vibration at frequencies of approximately 50 Hz. Analogous conclusions were published by Miniaci et al.,[20] who numerically studied the attenuation performance of three periodic configurations for low-frequency bulk and surface waves, showing that only periodic structures with a lattice constant at decameter dimensions could generate band gaps below 10 Hz.

Conversely, locally resonant structures consisting of inclusions embedded in a matrix can interact with incident waves at a sub-wavelength scale.[1,5] Recently, researchers have proposed the feasibility of shielding surface seismic waves by arranging a periodic array of resonators or barriers on the soil surface. A series of interesting studies conducted by Colombi et al.[30] showed that the strong impedance mismatch and coupling of wave modes between surface waves and an array of trees could generate surface wave hybridization band gaps at approximately 40 Hz. Later, Colquitt and Colombi et al.[31,32] reported the initial idea of vertical sub-wavelength resonators distributed on infinite elastic half-space interacting with Rayleigh waves to mitigate surface ground motion, commonly known as “resonant metasurfaces” from their seminal works. According to the local resonance mechanism, Palermo et al.[33] designed soil-embedded resonators to block seismic surface waves below 10 Hz and theoretically and experimentally demonstrated the conversion of Rayleigh waves to shear bulk waves.

In addition, the heterogeneity of soil profile in practical engineering might induce elastic wave bending effects, frequently indicated as the “mirage” effect.[34] To consider the effect of substrate material inhomogeneity, Palermo et al.[35] numerically and experimentally investigated how sagittal polarized guided surface acoustic modes (GSAMs) interact with surface resonances in unconsolidated granular media. Later, Zaccherini et al.[36] further revealed the propagation and mitigation performance of Rayleigh-like waves in a granular medium equipped with multi-layer

sub-wavelength resonant metabarriers. Both the small-scale experiment and numerical simulation showed that the low-order GSAM could be strongly coupled to the metasurfaces at resonance, while all higher-order surface acoustic modes presented a down-conversion phenomenon, owing to the heterogeneity of the granular media. Moreover, Zeighami and Palermo et al.[37] numerically designed a locally resonant metabarrier placed over a heterogeneous soil surface to assess the attenuation performance of medium-size scale resonant barriers for seismic surface waves in the range of 50–100 Hz.

To the best of the Authors' konwledge, due to the high cost of resonator preparation and soil excavation engineering, the aforementioned studies mainly focused on describing the interaction of Rayleigh waves with vertical resonators in semi-infinite space based on analytical models and numerical simulations, or emphasizing vertically hybrid surface waves in inhomogeneous media through numerical analyses and small-scale experiments. In such case, some practical engineering problems, such as real site conditions, the effect of hysteretic damping and soil nonlinearity under dynamic excitations have not been fully considered so far. Although Pu et al.[38] have investigated the influence of resonant metasurfaces and fluid–solid interaction on surface wave propagation under groundwater level variations, an analytical framework for the coupling between Rayleigh waves and local resonators distributed on stratified soil surfaces has not been reported on the geophysical scale. In this study, we aim to investigate (i) the analytical solutions of the dispersion laws for local resonators placed atop a stratified soil surface, (ii) the interaction of Rayleigh waves with vertically resonant metasurfaces, and (iii) the attenuation performance of finite-length resonant metasurfaces.

The remainder of this paper is organized as follows. After reviewing the dynamic properties of periodic and locally resonant structures, an analytical model of resonant metasurfaces under practical engineering conditions is proposed, considering the propagation of Rayleigh waves through a stratified semi-infinite space equipped with local resonators in Section 1. Based on the classical elastodynamic theory and an effective medium approach, the dispersion equation of stratified soil–resonator interaction is derived in Section 2, and the eigen equation is simplified by recombining the Abo-zena algorithm and delta matrix method to avoid the problem of high-frequency effective digit loss. In Section 3, three types of unit cell FE models and transmission models with finite-length metasurfaces are designed, and the validity of the FE model is verified by comparison with those proposed in previous studies. In Section 4, to gain further insight into the resonator–surface wave coupling mechanism, the theoretical dispersion laws of stratified soil–resonators are plotted and validated again based on FE simulations. Additionally, the attenuation performance of finite-length metasurfaces is investigated in the frequency and time domains. We subsequently design a graded resonant metasurface with decreasing frequency and compare their isolation effectiveness with those of the reference models via time history analyses. Finally, concluding remarks are presented in Section 5.

Notation

ρ	=	density	C_{L}	=	longitudinal wave velocity
d	=	thickness		=	$\sqrt{(\lambda+2\mu)/\rho}$
λ, μ	=	Lame elastic constants	C_{S}	=	shear wave velocity
f	=	frequency		=	$\sqrt{\mu/\rho}$

c = phase velocity of the free wave along the x-axis

u = x component of displacement

w = z component of displacement

σ_z = normal stress

τ_{xz} = tangential stress

ω = $2\pi f$

k = ω/c

i = $\sqrt{-1}$

$$\gamma_L = \begin{cases} i\sqrt{(c/C_L)^2 - 1} & c > C_L \\ \sqrt{1-(c/C_L)^2} & c < C_L \end{cases}$$

$$\gamma_S = \begin{cases} i\sqrt{(c/C_S)^2 - 1} & c > C_S \\ \sqrt{1-(c/C_S)^2} & c < C_S \end{cases}$$

$\gamma = 2(C_S/c)^2$

$P = \exp(\gamma_L kd)$

$Q = \exp(\gamma_S kd)$

2 ANALYTICAL FRAMEWORK

In this section, we develop an analytical framework to derive the dispersion equation of Rayleigh waves in stratified soils interacting with surface resonators, numerically and experimentally, to investigate sagittal polarized GSAMs in unconsolidated granular media interacting with vertical surface oscillators.[35] Accordingly, we restrict the investigation to a two-dimensional (2D) plane strain problem in the x-z plane (see Figure (1a)). Consider a horizontally stratified elastic semi-infinite space with surface waves propagating along the x-axis. Each layer is assumed to be isotropic, homogeneous, and perfectly bonded at the interface, and its geometric and physical properties are shown in Figure 1(a). Additionally, numerous previous studies[30–33,35–38] have demonstrated that only the vertical resonance mode can open a significant surface wave band gap. Thus, the resonant metasurfaces are represented by a certain number of identical single-degree-of-freedom single mass–spring resonators in meter-size dimensions.

The dispersion laws of the hybrid Rayleigh waves are theoretically derived through an effective medium approximation and continuity of displacement and stress at the interface to guide the design of resonant metasurfaces. The procedures of the analytical framework are arranged as follows: (i) the displacements and stresses at the free surface caused by Rayleigh waves propagating in isotropic, linear elastic half-space, (ii) the dynamic response of a vertical oscillator subjected to harmonic base excitation, (iii) the eigen equation of Rayleigh waves interacting with surface resonators, and (iv) an improved algorithm for solving the eigen equation.

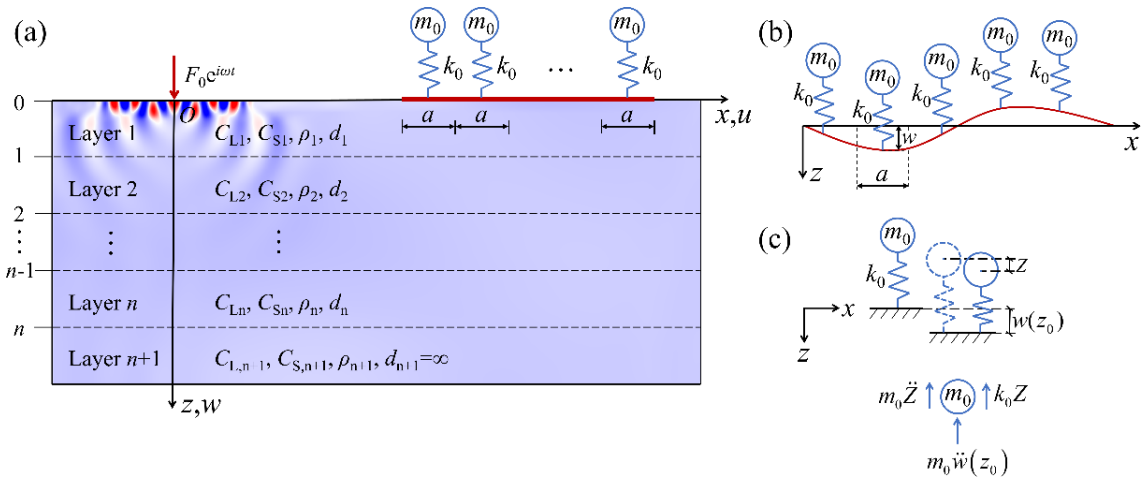

Figure 1. Schematic of the resonant metasurfaces. (a) Rayleigh waves interacting with surface resonators on stratified soils, with notations used in the theoretical model; (b) Physical model of the resonant metasurfaces; (c) Motion of representative single mass–spring resonator under vertical seismic excitation.

2.1 Waves motion in elastic media

The physical model is shown schematically in Figure 1(b). For isotropic, linear elastic media ignoring damping and body force, the governing equation of waves propagating in the soil substrate can be drawn by the displacement vector $\mathbf{u}(\mathbf{r})$:

$$(\lambda(\mathbf{r})+\mu(\mathbf{r}))\nabla(\nabla\cdot\mathbf{u}(\mathbf{r}))+\mu\nabla^2\mathbf{u}(\mathbf{r})=\rho(\mathbf{r})\frac{\partial^2\mathbf{u}(\mathbf{r})}{\partial t^2}, \tag{1}$$

where $\nabla=[\partial/\partial x,\partial/\partial z]$ is the differential operator, $\mathbf{u}(\mathbf{r})$ = [u, w] is the displacement vector, and t is the time. According to the Helmholtz decomposition, the vertical and horizontal displacement components u and w of the wave field can be expressed as

$$u=\frac{\partial\phi}{\partial x}-\frac{\partial\psi}{\partial z},\qquad w=\frac{\partial\phi}{\partial z}+\frac{\partial\psi}{\partial x}, \tag{2}$$

where ϕ and ψ are the scalar and vector potential functions of the dilatational and transverse components of the displacement, respectively, and those for a semi-infinite elastic domain take the following form:[39,40]

$$\nabla^2\phi=\frac{1}{C_L^2}\frac{\partial^2\phi}{\partial t^2},\qquad \nabla^2\psi=\frac{1}{C_S^2}\frac{\partial^2\psi}{\partial t^2}. \tag{3}$$

Assuming harmonic waves traveling along the x-axis with angular frequency ω and wavenumber k and recognizing that the waves are plane, the potential functions can be considered as

$$\phi(x,z,t)=\phi_0(z)\exp[i(\omega t-kx)], \tag{4a}$$

$$\psi(x,z,t)=\psi_0(z)\exp[i(\omega t-kx)]. \tag{4b}$$

Substituting Equation (4a) and (4b) into Equation (3) yields two uncoupled equations:

$$\frac{d^2\phi_0}{dz^2} = k^2\left(1-\frac{c^2}{C_L^2}\right)\phi_0 , \tag{5a}$$

$$\frac{d^2\psi_0}{dz^2} = k^2\left(1-\frac{c^2}{C_S^2}\right)\psi_0 . \tag{5b}$$

Solutions to Equation (5a) and (5b) are

$$\phi_0(z)=a_1\exp(\gamma_L kz)+a_2\exp(-\gamma_L kz)=\phi^+(z)+\phi^-(z) , \tag{6a}$$

$$\psi_0(z)=b_1\exp(\gamma_S kz)+b_2\exp(-\gamma_S kz)=\psi^+(z)+\psi^-(z) , \tag{6b}$$

where the four unknown constants a_1, a_2, b_1, and b_2 appearing in Equation (6a) and (6b) are determined by the boundary conditions of each surface layer. For convenience, Equation (6a) and (6b) are expressed more concisely, where ϕ^+ and ψ^+ represent the up-going waves and ϕ^- and ψ^- represent the down-going waves.

Substituting Equation (6a) and (6b) into Equation (2) yields a set of equations relating the displacement components to ϕ^+, ϕ^-, ψ^+, and ψ^- as follows:

$$u = -ik\phi^+ - ik\phi^- - k\gamma_S\psi^+ + k\gamma_S\psi^- , \tag{7a}$$

$$w = k\gamma_L\phi^+ - k\gamma_L\phi^- - ik\psi^+ - ik\psi^- , \tag{7b}$$

from which the stresses σ_z and τ_{xz} can be expressed as follows:

$$\begin{aligned}\sigma_{zz} &= \lambda\nabla^2\phi + 2\mu\frac{\partial^2\phi}{\partial z^2} + 2\mu\frac{\partial^2\psi}{\partial x\partial z}\\ &= \left[\lambda(k^2\gamma_L^2-k^2)+2\mu k^2\gamma_L^2\right]\phi^+ + \left[\lambda(k^2\gamma_L^2-k^2)+2\mu k^2\gamma_L^2\right]\phi^- ,\\ &\quad -2i\mu k^2\gamma_S\psi^+ + 2i\mu k^2\gamma_S\psi^-\end{aligned} \tag{8a}$$

$$\begin{aligned}\tau_{xz} &= \mu\left(2\frac{\partial^2\phi}{\partial x\partial z}+\frac{\partial^2\psi}{\partial x^2}-\frac{\partial^2\psi}{\partial z^2}\right)\\ &= \mu\left[-2ik^2\gamma_L\phi^+ + 2ik\gamma_L\phi^- - (k^2+k^2\gamma_S^2)\psi^+ - (k^2+k^2\gamma_S^2)\psi^-\right]\end{aligned} , \tag{8b}$$

where the factor $\exp\left[i(\omega t-kx)\right]$ is suppressed in Equation (7) and (8).

2.2 Dynamics of surface resonators

The kinematic equation of a single mass–spring resonator subjected to the base excitation is expressed as follows:

$$m_0\left(\ddot{Z}+\ddot{w}(z_0)\right)+k_0Z=0 , \tag{9}$$

where m_0 is the resonator mass, k_0 is the vertical spring stiffness, Z denotes the relative motion of the mass with respect to the ground, and $w(z_0)$ the base displacement (and both are supposed to be positive in the downward z-direction, see Figure 1(c)).

A harmonic wave solution of the form $Z=Z_0\exp\left[i(\omega t-kx)\right]$ is assumed. Substituting the equation into Equation (9), we obtain the resonator displacement amplitude as follows:

$$Z_0=\frac{\omega^2}{\omega_0^2-\omega^2}w(z_0) , \tag{10}$$

where ω_0 is the angular resonance frequency. The Rayleigh wavelength at the angular resonance frequency is much larger than the mass–spring spacing a, that is, the resonator and its footprint length have sub-wavelength dimensions at the resonance frequency. Thus, an effective medium approximation method is introduced to approximate the uniform vertical pressure stress σ_z exerted by the mass–spring at the surface (z = 0) as the elastic force divided by

the area of the resonator foundation.

$$\sigma_z(z_0) = \frac{k_0 Z}{A} = \frac{\omega^2 \omega_0^2 m_0}{A(\omega_0^2 - \omega^2)} w(z_0), \tag{11}$$

where A is the area of each resonator foundation. For the surface resonators arranged in a square lattice in this study, $A = a^2$.

2.3 Eigen equation

Moreover, Equation (7) and (8) can be written in the matrix notation as

$$\mathbf{S}(z) = \mathbf{H}\mathbf{\Phi}(z), \tag{12}$$

where

$$\mathbf{S}(z) = \left[\frac{iu}{k} \quad \frac{w}{k} \quad \frac{\sigma_{zz}}{k^2 c^2} \quad \frac{i\tau_{xz}}{k^2 c^2} \right]^T, \tag{13a}$$

$$\mathbf{\Phi}(z) = \left[\phi^+(z) \quad \phi^-(z) \quad -i\psi^+(z) \quad i\psi^-(z) \right]^T, \tag{13b}$$

and $\mathbf{H}$ is a 4 × 4 matrix whose elements are a function of the elastic constants of the medium at each layer and phase velocity c, and independent of the frequency f (see Appendix). Thus, Equation (12) can be applied to each layer.

For the mth layer, according to the displacement characteristics of each layer in the positive z-direction, the relation between the four unknown coefficients at the boundary m and the boundary m-1 can be written as

$$\mathbf{\Phi}_m(z_m) = \mathbf{E}_m \mathbf{\Phi}_m(z_{m-1}), \tag{14}$$

where

$$\mathbf{E}_m = diag\left[P \quad \frac{1}{P} \quad Q \quad \frac{1}{Q} \right]_m, \qquad z_0 = 0. \tag{15}$$

By substituting Equation (12) into Equation (14), the stress displacement vector can be expressed as

$$\begin{aligned} \mathbf{S}_m(z_m) &= \mathbf{H}_m \mathbf{E}_m \mathbf{\Phi}_m(z_{m-1}) = \mathbf{H}_m \mathbf{E}_m \mathbf{H}_m^{-1} \mathbf{S}_m(z_{m-1}) \\ &= \mathbf{T}_m \mathbf{S}_m(z_{m-1}) \end{aligned}, \tag{16}$$

where

$$\mathbf{T}_m = \mathbf{H}_m \mathbf{E}_m \mathbf{H}_m^{-1}. \tag{17}$$

Owing to the continuity of the stress displacement vector at the boundary of any layer, Equation (16) can be further expressed as:

$$\mathbf{S}(z_n) = \mathbf{T}_n \mathbf{T}_{n-1} \cdots \mathbf{T}_1 \mathbf{S}(z_0) = \mathbf{K}\mathbf{S}(z_0), \tag{18}$$

where

$$\mathbf{K} = \mathbf{T}_n \mathbf{T}_{n-1} \cdots \mathbf{T}_1. \tag{19}$$

By substituting Equation (12) into Equation (18), we obtain

$$\mathbf{\Phi}_{n+1}(z_n) = \mathbf{H}_{n+1}^{-1} \mathbf{K} \mathbf{S}(z_0) = \mathbf{R}\mathbf{S}(z_0), \tag{20}$$

where

$$\mathbf{R} = \mathbf{H}_{n+1}^{-1} \mathbf{K}. \tag{21}$$

Equipped with the interaction of the surface wave with the resonators, the stress-free boundary condition for the semi-infinite medium is substituted with the vertical stress σ_z. In addition, there is no source at infinity, i.e., $\phi_{n+1}^{+}(z_n)=\psi_{n+1}^{+}(z_n)=0$. Thereafter, Equation (20) becomes

$$\begin{bmatrix} 0 \\ \phi_{n+1}^{-}(z_n) \\ 0 \\ i\psi_{n+1}^{-}(z_n) \end{bmatrix} = \begin{bmatrix} r_{11} & r_{12} & r_{13} & r_{14} \\ r_{21} & r_{22} & r_{23} & r_{24} \\ r_{31} & r_{32} & r_{33} & r_{34} \\ r_{41} & r_{42} & r_{43} & r_{44} \end{bmatrix} \begin{bmatrix} \dfrac{iu(z_0)}{k} \\ \dfrac{w(z_0)}{k} \\ \dfrac{\xi w(z_0)}{k} \\ 0 \end{bmatrix}, \tag{22}$$

where $\xi=\dfrac{k\omega_0^2 m_0}{A(\omega^2-\omega_0^2)}$, r_{ij} is the element of the matrix **R**.

By arranging the first and third equations in Equation (22), we obtain

$$\begin{cases} r_{11}\dfrac{iu(z_0)}{k}+\left[r_{12}+\xi r_{13}\right]\dfrac{w(z_0)}{k}=0 \\ r_{31}\dfrac{iu(z_0)}{k}+\left[r_{32}+\xi r_{33}\right]\dfrac{w(z_0)}{k}=0 \end{cases}. \tag{23}$$

To obtain the nontrivial solutions of Equation (23), the coefficient matrix **LS** can be calculated as

$$\det\left[\mathbf{LS}\right]=\begin{bmatrix} r_{11} & r_{12}+\xi r_{13} \\ r_{31} & r_{32}+\xi r_{33} \end{bmatrix}=0. \tag{24}$$

2.4 Improved matrix formulation

The eigen equations derived thus far constitute a closed-form solution to the problem, and a concise algorithm can be developed on this basis. Numerically, however, the coefficient matrix **LS** was unsatisfactory. The research results of Knopoff,[41] Dunkin,[42] and Thrower et al.[43] showed that there were serious precision difficulties in determining all the real roots of the characteristic determinant for a layered elastic half-space, and they proposed to overcome this problem by introducing a delta matrix algorithm. Additionally, Abo-zena[44] developed another method that not only avoids the persistent problem of loss of effective digits at high frequencies, but also improves the convergence speed. Accordingly, we improve the Abo-zena algorithm and delta matrix method to determine the hybrid Rayleigh wave dispersion of layered elastic medium without restriction on the loss of high-frequency effective digits, ensuring a higher computational efficiency.

As is evident, **LS** is only a 2 × 2 matrix formed by multiplying the first and third rows of the matrix $\mathbf{H}_{n+1}^{-1}$ and the first three columns of matrix **K**. Therefore, the first and third rows of the matrix $\mathbf{H}_{n+1}^{-1}$ can be denoted as

$$\begin{bmatrix} \mathbf{E}_{\mathrm{A}} \\ \mathbf{E}_{\mathrm{B}} \end{bmatrix}=\frac{1}{2}\begin{bmatrix} \gamma & -\dfrac{(\gamma-1)}{\gamma_{\mathrm{L}}} & -\dfrac{1}{\rho} & -\dfrac{1}{\rho\gamma_{\mathrm{L}}} \\ -\dfrac{(\gamma-1)}{\gamma_{\mathrm{S}}} & \gamma & \dfrac{1}{\rho\gamma_{\mathrm{S}}} & -\dfrac{1}{\rho} \end{bmatrix}. \tag{25}$$

Thereafter, the matrix **LS** can be expressed as

$$\mathbf{LS}=\begin{bmatrix}\mathbf{E}_{\mathrm{A}}\\ \mathbf{E}_{\mathrm{B}}\end{bmatrix}\mathbf{K}\begin{bmatrix}1 & 0\\ 0 & 1\\ 0 & \xi\\ 0 & 0\end{bmatrix}=\begin{bmatrix}[\mathbf{E}_{\mathrm{A}}]\mathbf{K}\begin{bmatrix}1\\0\\0\\0\end{bmatrix} & [\mathbf{E}_{\mathrm{A}}]\mathbf{K}\begin{bmatrix}0\\1\\\xi\\0\end{bmatrix}\\ [\mathbf{E}_{\mathrm{B}}]\mathbf{K}\begin{bmatrix}1\\0\\0\\0\end{bmatrix} & [\mathbf{E}_{\mathrm{B}}]\mathbf{K}\begin{bmatrix}0\\1\\\xi\\0\end{bmatrix}\end{bmatrix}, \tag{26}$$

233 from which Equation (24) can be rewritten as

$$\det[\mathbf{LS}]=[\mathbf{E}_{\mathrm{A}}]\mathbf{K}\begin{bmatrix}1\\0\\0\\0\end{bmatrix}[\mathbf{E}_{\mathrm{B}}]\mathbf{K}\begin{bmatrix}0\\1\\\xi\\0\end{bmatrix}-[\mathbf{E}_{\mathrm{A}}]\mathbf{K}\begin{bmatrix}0\\1\\\xi\\0\end{bmatrix}[\mathbf{E}_{\mathrm{B}}]\mathbf{K}\begin{bmatrix}1\\0\\0\\0\end{bmatrix}. \tag{27}$$

234 Using the transpose property of the matrix, we can obtain the eigen determinant as

$$\det[\mathbf{LS}]=\begin{bmatrix}1 & 0 & 0 & 0\end{bmatrix}\mathbf{K}^{\mathrm{T}}\left\{[\mathbf{E}_{\mathrm{A}}]^{\mathrm{T}}[\mathbf{E}_{\mathrm{B}}]-[\mathbf{E}_{\mathrm{B}}]^{\mathrm{T}}[\mathbf{E}_{\mathrm{A}}]\right\}\mathbf{K}\begin{bmatrix}0\\1\\\xi\\0\end{bmatrix}. \tag{28}$$

235

236 The related matrix can be further defined as $\mathbf{Y}_{n+1}=[\mathbf{E}_{\mathrm{A}}]^{\mathrm{T}}[\mathbf{E}_{\mathrm{B}}]-[\mathbf{E}_{\mathrm{B}}]^{\mathrm{T}}[\mathbf{E}_{\mathrm{A}}]$. More specifically,

$$\mathbf{Y}_{n+1}=\frac{1}{4}\begin{bmatrix}0 & \gamma^2-\frac{(\gamma-1)^2}{\gamma_{\mathrm{L}}\gamma_{\mathrm{S}}} & \frac{1}{\rho\gamma_{\mathrm{S}}} & -\frac{\gamma}{\rho}+\frac{\gamma-1}{\rho\gamma_{\mathrm{L}}\gamma_{\mathrm{S}}}\\ -\gamma^2+\frac{(\gamma-1)^2}{\gamma_{\mathrm{L}}\gamma_{\mathrm{S}}} & 0 & -\frac{\gamma-1}{\rho\gamma_{\mathrm{L}}\gamma_{\mathrm{S}}}+\frac{\gamma}{\rho} & -\frac{1}{\rho\gamma_{\mathrm{L}}}\\ -\frac{1}{\rho\gamma_{\mathrm{S}}} & \frac{\gamma-1}{\rho\gamma_{\mathrm{L}}\gamma_{\mathrm{S}}}-\frac{\gamma}{\rho} & 0 & \frac{1}{\rho^2}-\frac{1}{\rho^2\gamma_{\mathrm{L}}\gamma_{\mathrm{S}}}\\ \frac{\gamma}{\rho}-\frac{\gamma-1}{\rho\gamma_{\mathrm{L}}\gamma_{\mathrm{S}}} & \frac{1}{\rho\gamma_{\mathrm{L}}} & -\frac{1}{\rho^2}+\frac{1}{\rho^2\gamma_{\mathrm{L}}\gamma_{\mathrm{S}}} & 0\end{bmatrix}. \tag{29}$$

237 By substituting Equations (29) and (19) into Equation (28), we obtain

$$\det[\mathbf{LS}]=\begin{bmatrix}1 & 0 & 0 & 0\end{bmatrix}\mathbf{T}_1^{\mathrm{T}}\cdots\mathbf{T}_{n-1}^{\mathrm{T}}\mathbf{T}_n^{\mathrm{T}}\mathbf{Y}_{n+1}\mathbf{T}_n\mathbf{T}_{n-1}\cdots\mathbf{T}_1\begin{bmatrix}0\\1\\\xi\\0\end{bmatrix}. \tag{30}$$

238 Equation (30) can be expressed in a recursive format equivalent to

$$\mathbf{Y}_m=\mathbf{T}_m^{\mathrm{T}}\mathbf{Y}_{m+1}\mathbf{T}_m \qquad n,n-1,\cdots 1, \tag{31a}$$

$$\det[\mathbf{LS}]=\mathbf{Y}_1(1,2)+\xi\mathbf{Y}_1(1,3), \tag{31b}$$

239 where $\mathbf{Y}_1(1,2)$ and $\mathbf{Y}_1(1,3)$ represent the elements of row1, column2, and row1, column3, respectively, in matrix $\mathbf{Y}_1$.
240 From Equation (29), it follows that $\mathbf{Y}_{n+1}$ is an antisymmetric matrix; if $\mathbf{Y}_{n+1}$ is antisymmetric, then $\mathbf{T}_m^{\mathrm{T}}\mathbf{Y}_{m+1}\mathbf{T}_m$ is
241 also antisymmetric.
242

243 This indicates that the above recursive formulas still cannot overcome the loss of significant digits. Additionally,

because there are only six independent elements in the matrix $\mathbf{Y}_m$, Equation (31a) can be arranged in terms of operations on the matrix elements:

$$\hat{y}_{ij} = \sum_{l=1}^{4}\sum_{n=1}^{4} g_{li} y_{ln} g_{nj}\,, \tag{32}$$

where $\hat{y}_{ij}$, g_{li}, and y_{ln} are the elements of the matrix $\mathbf{Y}_m$, $\mathbf{T}_m$, and $\mathbf{Y}_{m+1}$, respectively. According to the property of the antisymmetric matrix, Equation (32) can be expressed as:

$$\begin{aligned}\hat{y}_{ij} = {} & (g_{1i}g_{2j} - g_{2i}g_{1j})y_{12} + (g_{1i}g_{3j} - g_{3i}g_{1j})y_{13} + (g_{1i}g_{4j} - g_{4i}g_{1j})y_{14} + (g_{2i}g_{3j} - g_{3i}g_{2j})y_{23} \\ & + (g_{2i}g_{4j} - g_{4i}g_{2j})y_{24} + (g_{3i}g_{4j} - g_{4i}g_{3j})y_{34}\end{aligned}\,. \tag{33}$$

Equation (33) can be written in vector form:

$$\mathbf{W}_m = \mathbf{W}_{m+1}\mathbf{T}_m^* \qquad m = n, n-1, \cdots, 1\,, \tag{34}$$

where $\mathbf{W}_m = \begin{bmatrix}\hat{y}_{12} & \hat{y}_{13} & \hat{y}_{14} & \hat{y}_{23} & \hat{y}_{24} & \hat{y}_{34}\end{bmatrix}$ and $\mathbf{W}_{m+1} = \begin{bmatrix}y_{12} & y_{13} & y_{14} & y_{23} & y_{24} & y_{34}\end{bmatrix}$. From the expression of the elements of the matrix $\mathbf{T}_m^*$ in Equation (33), it can be observed that each element of the matrix $\mathbf{T}_m^*$ is a 2 × 2 sub-determinant of the matrix $\mathbf{T}_m$, i.e., $\mathbf{T}_m^*$ refers to the delta matrix of $\mathbf{T}_m$.

Considering the property of the delta matrix, the matrix $\mathbf{T}_m^*$ can be expressed as

$$\mathbf{T}_m^* = \mathbf{H}_m^* \mathbf{E}_m^* (\mathbf{H}_m^{-1})^*\,, \tag{35}$$

where $\mathbf{H}_m^*$, $\mathbf{E}_m^*$, and $(\mathbf{H}_m^{-1})^*$ represent the delta matrices of $\mathbf{H}_m$, $\mathbf{E}_m$, and $\mathbf{H}_m^{-1}$, respectively.

By substituting Equation (35) into Equation (34), we obtain the system

$$\mathbf{W}_m = \frac{1}{4}\mathbf{W}_{m+1}\mathbf{H}_m^*\mathbf{E}_m^*(\mathbf{H}_m^{-1})^* \qquad m = n, n-1, \cdots, 1\,, \tag{36}$$

where the initial vector $\mathbf{W}_m$ in Equation (36) can be expressed as

$$\mathbf{W}_{n+1} = \left[\gamma^2 - \frac{(\gamma-1)^2}{\gamma_{\mathrm{L}}\gamma_{\mathrm{S}}} \quad \frac{1}{\rho\gamma_{\mathrm{S}}} \quad -\frac{\gamma}{\rho} + \frac{\gamma-1}{\rho\gamma_{\mathrm{L}}\gamma_{\mathrm{S}}} \quad \frac{\gamma}{\rho} - \frac{\gamma-1}{\rho\gamma_{\mathrm{L}}\gamma_{\mathrm{S}}} \quad -\frac{1}{\rho\gamma_{\mathrm{L}}} \quad \frac{1}{\rho^2} - \frac{1}{\rho^2\gamma_{\mathrm{L}}\gamma_{\mathrm{S}}}\right]_{n+1}\,. \tag{37}$$

Therefore, the characteristic Equation (31b) can be further written as

$$\mathbf{W}_1(1,1) + \xi\mathbf{W}_1(1,2) = 0\,, \tag{38}$$

where $\mathbf{W}_1(1,1)$ and $\mathbf{W}_1(1,2)$ represent the elements of row1, column1, and row1, column2, respectively, in matrix $\mathbf{W}_1$. Incidentally, if n is set to zero, Equation (38) is reduced to the dispersion relation of the interaction between the resonant metasurfaces and Rayleigh waves propagating in an idealized elastic half-space.[33]

$$\left(\frac{\omega^2}{\omega_0^2} - 1\right)\left[\left(2 - \frac{\omega^2}{k^2 C_{\mathrm{S}}^2}\right)^2 - 4\sqrt{1 - \frac{\omega^2}{k^2 C_{\mathrm{L}}^2}}\sqrt{1 - \frac{\omega^2}{k^2 C_{\mathrm{S}}^2}}\right] = \frac{\omega^4 m_0}{A\rho k^3 C_{\mathrm{S}}^4}\sqrt{1 - \frac{\omega^2}{k^2 C_{\mathrm{L}}^2}} \tag{39}$$

3 FE MODEL AND VALIDATION

Before proceeding with any numerical simulation related to the dispersion of stratified soil, it is necessary to choose the appropriate site condition characterizing the mechanical properties of each soil stratum. Cai et al.[45] have reported the attenuation performance of 1D layered periodic trenches embedded in stratified soil and its application in train-induced ground vibration damping. Thus, the depth-dependent speed profiles were considered in this study, as shown in Table 1.

Moreover, three types of 2D unit cell FE models and a transmission calculation model, developed in COMSOL

Multiphysics, were designed to confirm the analytical dispersion relation and obtain further insights into the resonator–surface wave coupling mechanism. Accordingly, we first verified the accuracy of the Bloch-wave FE method by comparing it with the numerical results published by Palermo et al.[46] Furthermore, the attenuation of surface waves inside the frequency band gap was also validated by performing a transmission analysis of an array of metasurfaces distributed on the surface of the ground in the frequency domain.

Table 1. Soil stratification and mechanical parameters.[45]

No.	Soil type	Thickness d (m)	Density ρ (kg/m^3)	Shear wave speed C_S (m/s)	Longitudinal wave speed C_L (m/s)
1	Miscellaneous fill	4.6	1810	80.92	40.76
2	Plasticized silty clay	6.0	1850	117.99	60.71
3	Hard-plasticized granite residual soil	3.4	1950	125.05	65.62
4	Completely weathered granite	16.8	2100	121.89	70.37
5	Strongly weathered granite	9.2	2200	126.77	74.15

3.1 Unit cell design

Three configurations of the FE model were considered in the dispersion analysis: a stratified soil system with a stress-free boundary condition (BC) at the top, labeled as Unit cell A; a portion of homogeneous soil coupled with point mass–spring resonators, denoted as Unit cell B; and a unit cell C of the stratified soil–resonator interaction. For the stratified soil system (see Figure 2(a)), the unit cell has a width $w = a/10$ and a height $h = 40$ m to accurately identify surface wave modes around the resonant frequency. The soil stratification and mechanical parameters are provided in Table 1. In the numerical simulation, the unit cell substrate domain was discretized into triangular elements with quadratic Lagrange shape functions. In addition, we used the discretization of 10 elements for the minimum wavelength at the highest frequency of interest,[47,48] that is, $d_{\min} = C_R / f_{\max} / 10$, where C_R is the Rayleigh velocity and $f_{\max}$ is the highest frequency of interest in this study.

Owing to the periodicity of the model, Bloch–Floquet BCs were applied to the lateral edges of the unit cell to simulate an infinite array of the stratified soil system along the direction of wave propagation and fixed BCs to the bottom edge to avoid undesired rigid motions. It is observed that the dispersion relation is an implicit function of the wavenumber k and eigen frequency f. The corresponding eigen frequency can be solved based on the FE approaches reported by Phani et al.[49] by changing across the wave numbers in the boundary of the first irreducible Brillouin zone. Thereafter, a post-processing method reported by Huang et at.[50] is implemented to automatically identify the numerical surface wave solutions from all the Bloch modes.

The Unit cell B and C (see Figure 2(b) and (c)) have the same geometric size and mesh quality attributes as Unit cell A, except for the substitution of the standard zero-stress BCs with the previously discussed metasurface stresses. To simulate the uniform vertical stress imposed on the resonator foundation, a single mass–spring resonator was

dispersed over a set of 10 truss elements, as described in Ref 46, resulting in each point mass m_t = m_0/100 and Young's modulus of each truss $E = \omega_0^2 m_0 / S / 100$, where S is the cross-sectional area of the truss element. Additional point masses are also used to model the resonator mass borne by each truss element.

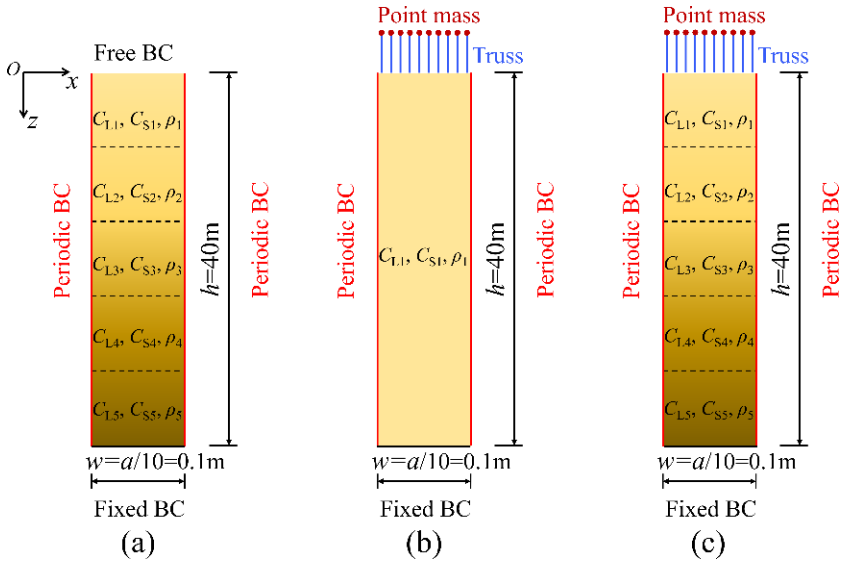

Figure 2. Schematic of unit cell FE model for dispersion analysis. (a) A stratified soil system with free BC at the top; (b) A homogeneous soil system coupled with a set of single mass–spring resonators; (c) A stratified soil system coupled with a set of single mass–spring resonators.

3.2 Transmission model design

A 2D strip model with a finite array of resonators under plane-strain conditions was developed to assess the attenuation efficiency of the resonant metasurfaces placed atop a stratified soil surface, as schematically shown in Figure 3. When the surface waves propagate in the first-layered soil, the velocity of the Rayleigh waves can be approximated as $C_R \approx (0.87+1.12\nu)\, C_S / (1+\nu)$ = 38 m/s. The frequency range for frequency domain analysis is 1–10 Hz. Therefore, the Rayleigh wavelength for the first-layered soil at the resonance frequency is expressed as $\lambda_{\omega R} = C_R / f_0$, where f_0 is the resonance frequency of the resonator. The computational domain has a depth of 5 $\lambda_{\omega R}$ and a total length of 18 $\lambda_{\omega R}$ + 2 l_{bar}, where l_{bar} represents the distribution length of the metasurfaces. The incident surface wave was generated by applying a vertical harmonic displacement ($w(f) = w_0 e^{i\omega t}$, w_0 = 0.01m). It should be emphasized that the source displacement generates both Rayleigh waves traveling along the free surface and bulk waves in the soil substrate, but the surface displacements in the far-field are dominated by Rayleigh waves, ensuring surface wave interaction with surface resonators.

Triangular elements with quadratic Lagrange shape functions were also applied to discretize the field domain, and the mesh quality was consistent with the unit cell FE model. To avoid numerical oscillation near the resonance frequency, all the elements were assigned a small isotropic loss factor (that is, ζ = 0.05). Additionally, perfectly

matched layers (PMLs) were employed at both the lateral and the bottom of the substrate to prevent undesired reflections from the domain boundaries.

To evaluate the attenuation effect of the metasurfaces, the acceleration reduction spectrum (ARS) is defined as

$$\mathrm{ARS} = 20\log_{10}\frac{\int_0^{2\lambda_{\omega R}}\left|a_{\mathrm{z,with}}\right|dx}{\int_0^{2\lambda_{\omega R}}\left|a_{\mathrm{z,without}}\right|dx}, \tag{40}$$

where $a_{\mathrm{z,with}}$ represents the vertical acceleration component extracted from output1, $a_{\mathrm{z,without}}$ is the reference acceleration field obtained from the left side of the domain (Output2). Note that the ARS is negative if $a_{\mathrm{z,with}}$ is less than $a_{\mathrm{z,without}}$ that indicates that metasurfaces mitigate the ground vibration.

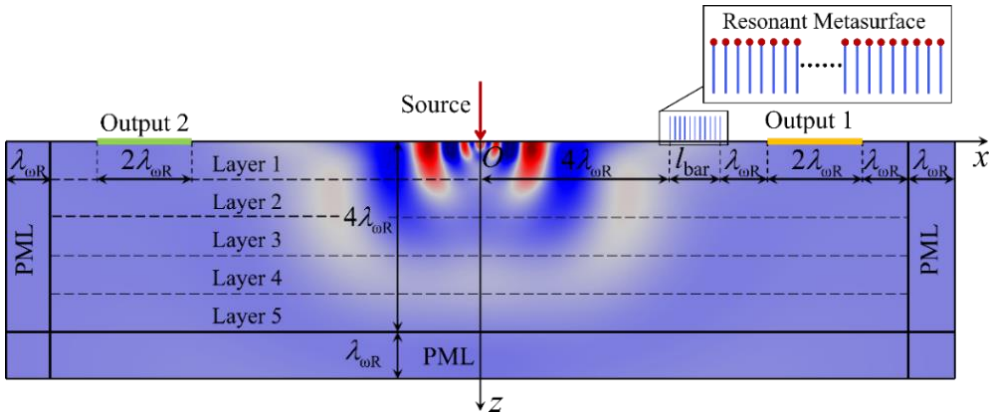

Figure 3. Schematic of the 2D plane-strain FE model geometry. The computational domain on the right represents a finite number of mass–spring resonators attached to the free surface of a stratified soil system, while that on the left represents surface waves propagating along the free surface subjected to harmonic excitation.

3.3 Comparison and validation

To substantiate the feasibility of the FE models, the problem of surface waves interacting with resonant matabarriers reported by previous researchers is reconsidered.[46] The upper panel of Figure 4(a) shows the dispersion curves for sedimentary soil coupled with a single-mass metabarrier. The unit cell has a width $w = A/(1\mathrm{m})/10$ and a height $h = 4\lambda_{\omega r}$, where $\lambda_{\omega r}$ is the Rayleigh wavelength at $f = 2.43$ Hz. The relationship between the transmission coefficient and excitation frequency obtained in this study was also compared with that in previous research, as depicted in the lower panel of Figure 4(a). In transmission analysis, the considered metabarrier has a length $L_{\mathrm{res}} = \lambda_{\omega r}$, with resonator mass $m = 10500$ kg and resonance frequency $f_{\mathrm{r}} = 2.43$ Hz. Evidently, the surface wave dispersion curves and transmission spectra obtained in the present study agree well with those in previous studies.

Furthermore, it should be noted that the attenuation peak of the transmission spectrum deviates from the surface wave band gap (gray shaded area) and appears in the frequency region below the resonance frequency, where the surface waves are strongly hybridized with the resonant metabarrier. Figure 4(b) displays the nephogram of the

vertical displacement field generated by harmonic excitation at 2.21 Hz, 2.43 Hz, and 4 Hz. Apparent mode conversion of Rayleigh waves into bulk shear waves is observed at the frequency corresponding to the attenuation peak (2.21 Hz) that again validates the accuracy of the FE model. This phenomenon is further discussed in Section 4.

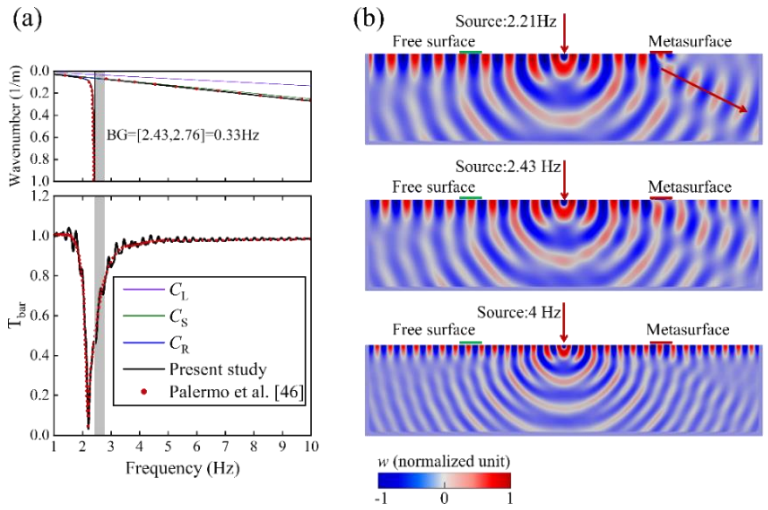

Figure 4. Comparative study of dispersion laws and transmission spectra of surface waves interacting with resonators arranged on homogeneous soil surface. (a) Dispersion curves and corresponding acceleration reduction spectrum; (b) The nephogram of vertical displacement field generated by harmonic excitation at 2.2 Hz, 2.43 Hz, and 4 Hz.

4 RESULTS AND DISCUSSION

4.1 Dispersion analysis

According to the mechanical parameters in Table 1, the first three–order surface wave modes (frequency versus wave number) of Unit cell A in the range of 1–10 Hz are theoretically and numerically calculated (see Figure 5(a)), along with the dispersion curves in terms of phase velocity versus frequency, as plotted in Figure 5(b). Note that the theoretical dispersion curves that are solutions of Equation (40) (that is, $\xi = 0$), are shown as solid lines in three colors (for example, M1–M3), while solid pink circles represent the FE surface wave solutions. As reported by Graff,[39] multiple surface modes are induced by the presence of stress-free BC and inhomogeneous elastic properties of the stratified soil system. Additionally, the analytical solutions show excellent agreement with the numerical results, confirming the accuracy of the Bloch-wave FE approach again.

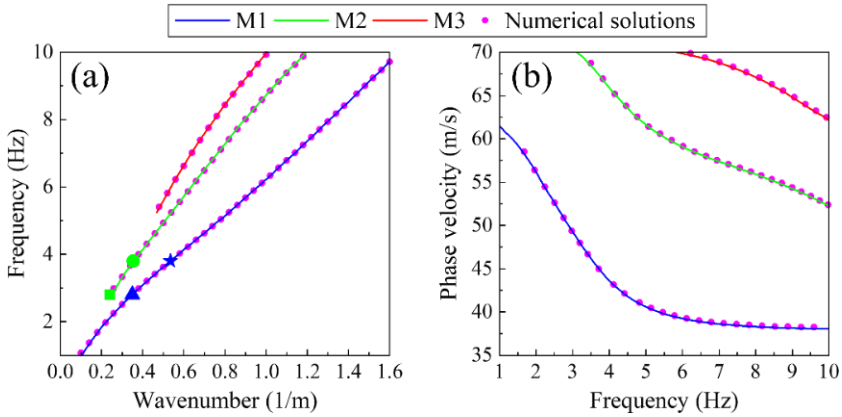

Figure 5. Dispersion curves for Unit cell A in terms of (a) frequency versus wavenumber and (b) phase velocity versus frequency.

The dispersion curves for vertically polarized surface waves in a stratified soil system are displayed, and the mechanical parameters of the soil and surface resonator are specified in Table 1 and Table 2, respectively. It should be noted that each resonance frequency f_0 of the resonator is crucial for the mitigation of surface seismic waves below 10 Hz that cover the most energetic frequencies of seismic spectra. Specifically, for a mass of m_0 and resonant frequency f_0, the compression stiffness of each resonator is $k_0 = m_0(2\pi f_0)^2$. Figure 6(a) and (b) show the analytical dispersion curves and FE solutions for Unit cell C in terms of frequency versus wavenumber and phase velocity versus frequency, respectively. This indicates that the FE solutions agree well with the analytical predictions. The vertical resonance of the resonator is plotted in Figure 6 by the gray dashed line. The first insight into the main features of the dispersion curves indicates that a highly localized mode (that is, M1) arises because of the coupling between Rayleigh waves and the metasurfaces, resulting in a flat dispersive branch at the resonance of the vertical resonator.

To emphasize the localization mechanism induced by the heterogeneous elastic properties, the analytical dispersion curves of a homogeneous soil system coupled with a resonant metasurface (Unit cell B), denoted by the solid cyan line, are also superimposed in Figure 6 (a). The mechanical parameters of the homogeneous soil are derived from the first layer in Table 1. It is observed that the Rayleigh waves in infinite elastic half-space hybridize with the vertical resonators at resonance, exhibiting a characteristic “avoided crossing” behavior. The dispersion curves are split into two repelling branches around the resonance frequency that results in a narrow surface wave band gap, as depicted in the gray area in Figure 6 (a). Within the frequency band gap, the propagation of Rayleigh waves is mitigated, and surface waves deviate from the stress-free surface in the form of shear vertically polarized waves, similar to what was observed in previous studies.[33,46] However, this behavior is not observed in the case of stratified soil configuration. Although the presence of vertical oscillators results in a flat branch for the first-order surface modes of a stratified soil system that is akin to the lower branch of a homogeneous soil system, the surface wave band gap is permeated by higher-order surface modes, that is, the frequency band gap disappears.

Table 2. Mechanical parameters of the surface resonator.

Parameter	Value
Mass, m_0	400 kg
Stiffness, k_0	2.5266×10^5 N/m
Resonance frequency, f_0	4 Hz
Lattice constant, a	1 m

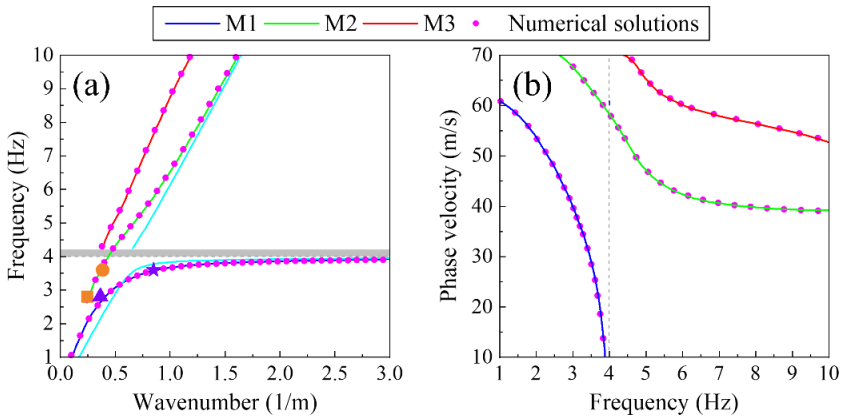

Figure 6. Dispersion curves for Unit cell C in terms of (a) frequency versus wavenumber and (b) phase velocity versus frequency. The superimposed solid cyan lines in panel (a) are the dispersion curves of a homogeneous soil system coupled with resonant metasurfaces.

For this reason, the normalized vertical displacement amplitudes of Unit cell A and C changing with the depth profile below the resonant frequency were extracted to emphasize the hybridization degree of surface waves by the metasurfaces, as plotted in Figure 7. The vertical displacement data at different frequency–wavenumber values are extracted from the dispersion curves in Figure 5(a) and Figure 6(a), where the Rayleigh (R) and hybrid Rayleigh (Rh) wave shapes represent the surface waves propagating in Unit cell A and C, respectively. The vertical displacement amplitude of the first-order R-wave at different frequency wavenumbers does not change significantly, and the trend of the attenuation changes with depth is basically the same. In contrast, the vertical displacement of the Rh-wave near the resonance frequency (that is, (k, f) = (0.85,3.8)) is confined to a thin layer, and the amplitude decays rapidly with depth further away from the free surface. Similar results (see Figure 7(b) and (e)) can be seen from the vertical displacement distribution of the second-order R-wave and Rh-wave along the depth. It can be asserted that such a phenomenon is the result of hybridization between the fundamental surface mode and metasurfaces that interact with an inhomogeneous elastic medium and gradually restrict the energy to the near-surface.

To investigate the coupling level of each order of surface modes with the metasurfaces, the vertical displacement fields of the first two order R and Rh waves close to the resonance frequency (that is, f = 3.8 Hz) were also compared, as shown in Figure 7(c) and (f). As shown in Figure 7(c), the vertical displacement amplitudes of the two modes are similar at the free surface, but the vertical displacement component of the first-order mode decays faster in the perpendicular direction than that of the second-order mode. Similar results can be observed in Figure 7(f). It can be concluded that only the fundamental surface mode can strongly couple to the resonant metasurfaces owing to the significant disappearance of the vertical displacement component at the free surface. Thus, it can be predicted

that these higher-order modes do no affect on the surface wave attenuation near the resonance frequency of metasurfaces.

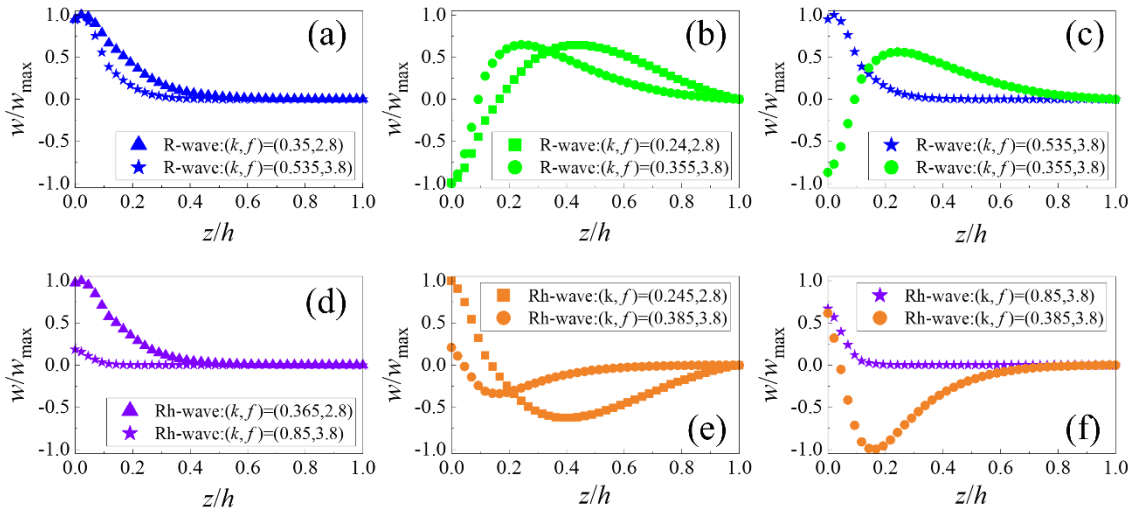

Figure 7. Normalized vertical displacement amplitude of surface modes of Unit cell A and C changing with depth.

4.2 Harmonic analysis

4.2.1 Frequency domain

In this section, the transmission efficiency of a finite number of surface resonators based on harmonic analysis is performed to validate the dispersion analysis predictions and obtain further insight into the attenuation performance of the stratified soil–resonator interaction.

The ARS and corresponding dispersion curves for surface resonators arranged on the surface of homogeneous and stratified soil configurations were calculated (see Figure 8), respectively, to assess the attenuation performance of the metasurfaces. Figure 8(a) shows a significant acceleration amplitude attenuation near the resonant frequency owing to the local resonance or wave hybridization mechanism. As initially proposed by Boechler et al.[51] and later by Palermo et al.,[33,46] within the frequency band gap (gray shaded area in Figure 8(a)), Equation (39) has no real mathematical root and the corresponding solutions exist in the region below the shear wave (solid green line in Figure 9(a)) in the form of hybrid Rayleigh waves. The incident Rayleigh waves near the resonant frequency are either captured by the resonant metasurfaces or forced to propagate downward as hybrid Rayleigh waves with different phase velocities, thus reducing ground motion. Simultaneously, the offset phenomenon of the attenuation peak can be explained by the previous studies wherein Rayleigh waves and hybrid Rayleigh waves have been poorly coupled at the metasurfaces.[32,46] Similarly, a prominent peak reduction can also be observed near the metasurface resonance in Figure 8(b) that can be attributed to the confinement of the first-order surface mode.

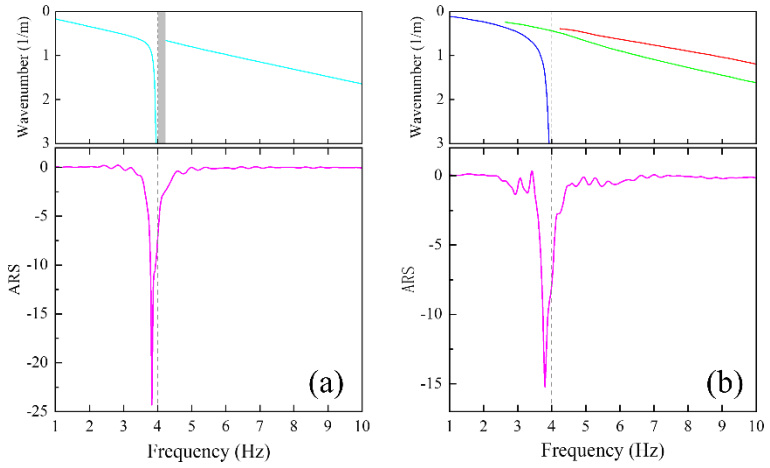

Figure 8. Analytical dispersion curves and corresponding transmission spectra under different soil types. (a) homogeneous soil and (b) stratified soil.

Moreover, the harmonic responses (vertical displacement fields) of homogeneous and stratified soil systems with and without metasurfaces are plotted in Figure 9 and 10, respectively. Specifically, Figure 9(b), (c), and (d) present the nephograms of the vertical displacement field generated by harmonic excitation at 3.84 Hz, 4 Hz, and 5 Hz. It can be observed that the incident Rayleigh waves near the resonant frequency (that is, 3.84 Hz and 4 Hz) cause a strong local resonance, resulting in a π phase shift of the incident waves that is converted into shear waves at the metasurface edges and transferred to the underground. In contrast, the vertical displacement field generated by harmonic excitation at 5 Hz (see Figure 9(b)) is basically consistent with the reference model on the left, demonstrating that Rayleigh waves outside the band gap can propagate through the metasurfaces.

Regarding the stratified soil–resonator configuration, it can be found from Figure 10(b), (c), and (d) that most of the wave energy is concentrated in the first layer because of the reflection of the elastic wave at the interface. However, this peculiar soil stratification and stiffness profile have a negligible effect on the trapping ability of the resonant metasurfaces. Considering the vertical displacement field under 3.8 Hz harmonic excitation as an example, the local resonance of the surface resonators can still capture most of the wave energy, leading to the reduction of ground vibration within a finite length behind the metasurfaces, as shown in Figure 10(d). For comparison, we also present the vertical displacement field of a stratified soil system with and without metasurfaces at 5 Hz, as plotted in Figure 9(b). No apparent phenomena such as surface wave–resonance interaction and surface-to-shear wave conversion were observed.

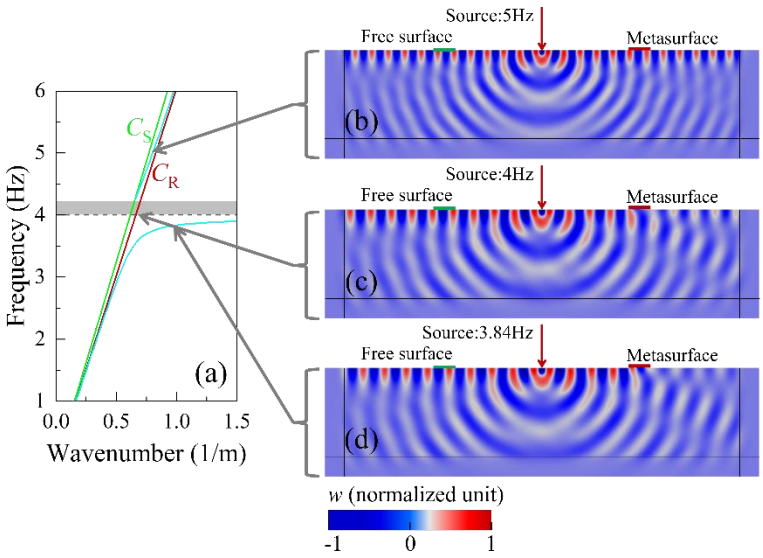

Figure 9. (a) Magnification of the dispersion curves of a homogeneous soil system coupled with resonant metasurfaces. The dispersion relation for both the shear wave (solid green line) and Rayleigh wave (solid red line) in the homogeneous elastic half-space are also superimposed in panel (a). (b) The nephogram of vertical displacement field generated by harmonic excitation at 3.84 Hz, 4 Hz, and 5 Hz.

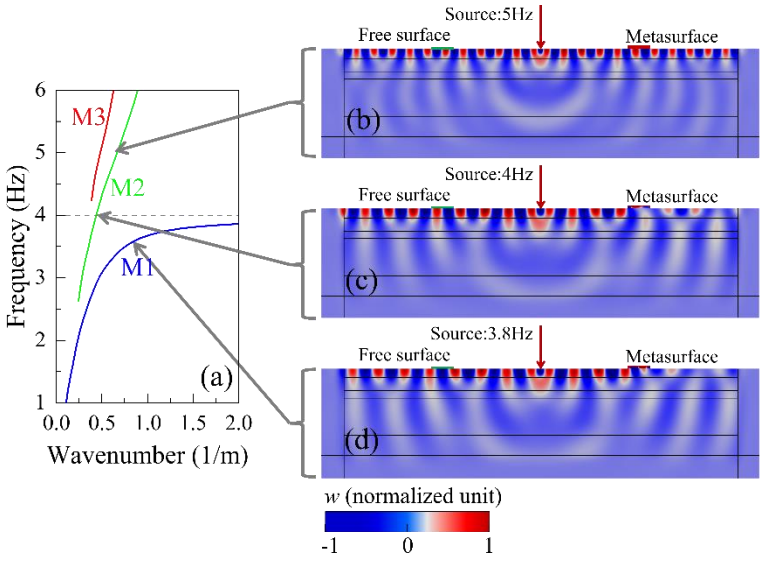

Figure 10. (a) Magnification of the dispersion curves of stratified soil–resonator interaction and (b) nephogram of vertical displacement field generated by harmonic excitation at 3.84 Hz, 4 Hz, and 5 Hz.

Parametric analyses, including resonator mass m_0 and arrangement length l_{bar}, were performed to investigate the attenuation capabilities of the metasurfaces. Keeping the resonance frequency of the resonator unchanged, Figure 11(a) presents the attenuation performance of the surface resonators with different masses. It is observed that both

the attenuation peak and starting frequency shift to lower frequencies, resulting in a larger attenuation domain for the surface resonator. Therefore, increasing the resonator mass can widen the ARS and thus induce more broadband performance for the metasurfaces. Simultaneously, another parametric study with different metasurface lengths was conducted to assess the minimum surface wave barrier length required for significant ground attenuation. We performed transmission analyses with different lengths of 0.2 $\lambda_{\omega R}$, 0.5 $\lambda_{\omega R}$, and $\lambda_{\omega R}$, and with a constant mass m_0 = 400 kg and k_0 = 2.5266 × 10^5 N/m for each resonator, as shown in Figure 11(b). As expected, the vertical acceleration responses at the output area decreased significantly as the metasurface length increased. In particular, for a metasurface length of l_{bar} = 0.5 $\lambda_{\omega R}$, an approximately 30% reduction (that is, ARS = -10) of surface ground motion is observed, indicating adequate attenuation performance of surface resonators.

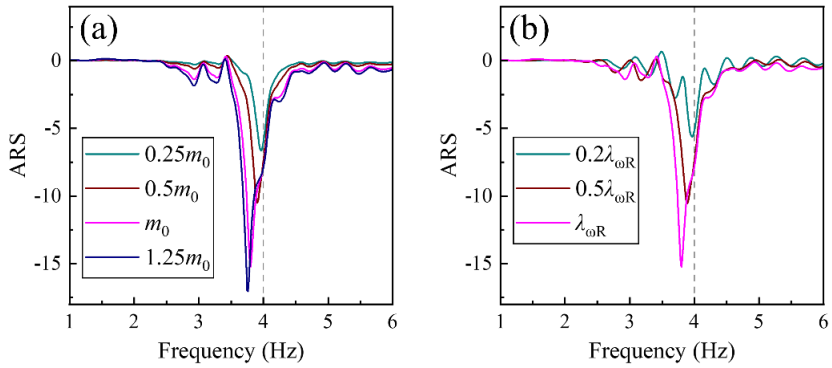

Figure 11. Effects of different parameters on acceleration reduction spectra. (a) Resonator mass (in this study, m_0 = 400 kg) and (b) Metasurface distribution length.

4.2.2 Time domain

Time-transient harmonic numerical simulations were also performed to further validate the numerical predictions of the dispersion analyses and to investigate the wave attenuation capability of vertical oscillators near resonance. In order to avoid undesired wave reflection, low reflection boundary conditions (LRBCs) are applied to the outside of the PML layers that are proven to be more effective in absorbing the propagating shear and longitudinal waves at the truncated boundaries in transient analysis.[37] Simultaneously, the bottom corners of the model are fixed, and three input signals with 2 Hz, 4 Hz, and 6 Hz are considered (see Figure 12). Surface waves are excited at the source point by utilizing a normalized harmonic acceleration in the *z*-direction. To avoid spurious oscillations at the onset, the normalized acceleration amplitude is modulated by a Heaviside step function, as follows:

$$A_{in}=\begin{cases}\dfrac{1}{A_{\max}}\left[1-\cos\left(\dfrac{2\pi f_c t}{C}\right)\right]\sin(2\pi f_c t) & \text{for} \quad 0\le t<\dfrac{C}{f_c},\\ 0 & \text{for} \quad t\ge\dfrac{C}{f_c}.\end{cases} \tag{41}$$

where $A_{\max}$ is the maximum signal amplitude, f_c is the central frequency of the applied pulses, C is the number of wave cycles, and t is the time duration. Such excitation is chosen to highlight the isolation performance of the designed metasurfaces, emphasizing that strong coupling occurs around the resonator resonance. In addition, the FE model used for transient analysis was consistent with the description of the transmission model, as shown in Figure

3.

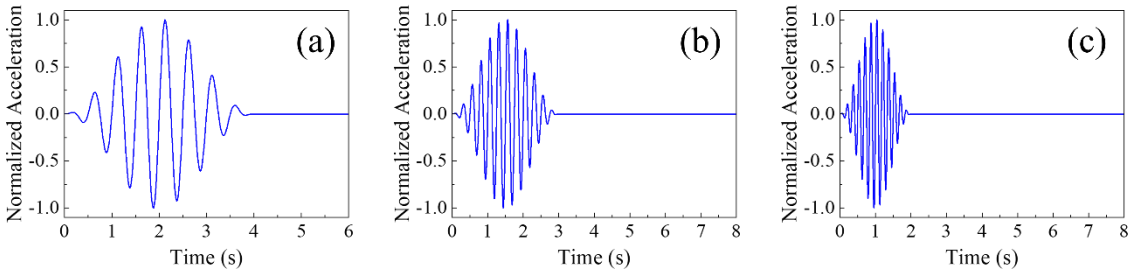

Figure 12. Normalized input wave signal. (a) f_c = 2 Hz, C = 8; (b) f_c = 4 Hz, C = 12; and (c) f_c = 6 Hz, C = 12.

The normalized average vertical acceleration responses at the detection area (that is, Output 1 and Output 2) were recorded and compared, as shown in Figure 13. The dashed and solid lines denote the results obtained with and without metasurfaces, respectively. As shown in Figure 13(b), the vertical acceleration responses at the output domain with metasurfaces are significantly smaller than those of signals without metasurfaces, owing to the generation of local resonance. When the center frequency of the input signal f_c = 4 Hz, the average vertical acceleration amplitude decreases by approximately 30% compared with the reference free surface. The output signals far from the resonant frequencies are plotted, as shown in Figure 13(a) and (c). It can be observed that the amplitudes of the time transient acceleration at the detection area are almost the same in both configurations (with and without resonators). Again, the transient analysis results confirm that the considerable amplitude reduction observed around the resonant frequency is caused by the strong coupling between the surface waves and metasurfaces.

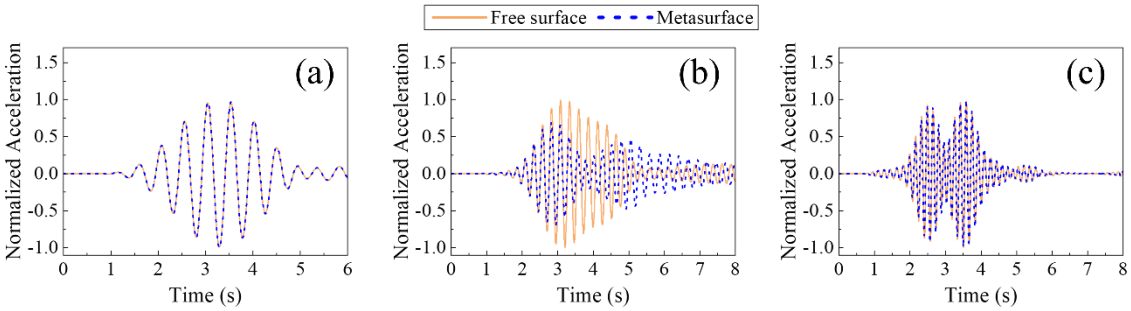

Figure 13. Normalized average vertical acceleration response at the output area. (a) f_c = 2 Hz, C = 5; (b) f_c = 4 Hz, C = 12; (c) f_c = 5 Hz, C = 10; and (d) f_c = 12 Hz, C = 12.

4.3 Attenuation efficiency of a graded metasurface

As mentioned above, the resonance frequencies of the metasurface were reasonably tailored to achieve considerable attenuation. To obtain attenuation at ultralow frequencies and a wider frequency range, the classic gradient metawedge presented by Colombi and Colquitt et al.[31] with decreasing frequencies along the propagation direction

is reconsidered. Note that a decreasing frequency metasurface can be modeled by linearly modifying the mass or spring stiffness of the vertical oscillators. Therefore, a decreasing-frequency case is adopted by linearly increasing the masses from 200 to 800 kg and maintaining the spring stiffness k_0 at 2.5266×10^5, as depicted in Figure 14(a). Figure 14(b) displays the acceleration attenuation spectra of the gradient metasurfaces in the frequency range of 1–10 Hz. The shaded area represents the corresponding resonance frequencies in the range of 2.82 Hz to 5.65 Hz. A wider attenuation zone and a more significant attenuation effect can be visually observed in the case of a resonant metasurface with a decreasing frequency compared with a constant frequency.

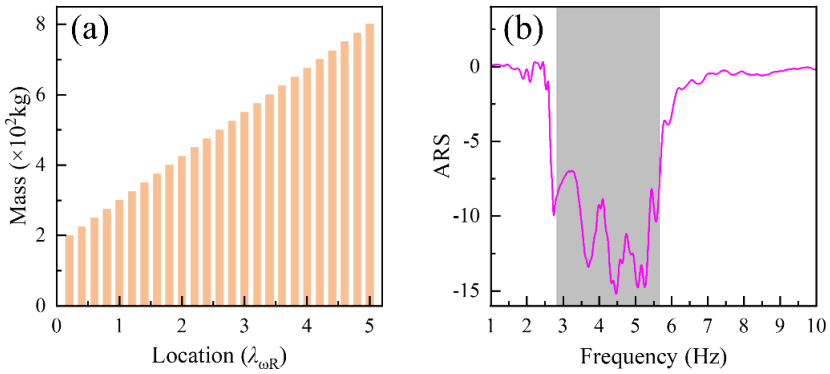

Figure 14. (a) Schematic of the mass distribution of graded metasurfaces for a constant stiffness of the resonators and (b) corresponding acceleration reduction spectra. The considered graded metasurfaces have a length $l_{bar} = 5\lambda_{\omega R}$ and stiffness $k_0 = 2.5266 \times 10^5$ N/m.

Furthermore, it is important to scrutinize the attenuation effect of the graded resonant metasurfaces via time-domain analyses with a natural seismic acceleration record. Thus, three accelerograms recorded from the Pacific Earthquake Engineering Research Ground Motion Database[52] were selected: Imperial Valley, Northridge, and L'Aquila as seismic inputs. Figure 15 depicts the time history and corresponding Fourier spectra of the three ground vibrations. Figure 15(b) shows that the dominant frequencies of the Imperial Valley earthquake are in the range of 1–6 Hz that is consistent with the attenuation zones of the graded metasurfaces and is expected to achieve significant shielding performance. However, the main frequency bands of the other two seismic records are relatively scattered, and there are still large vibration amplitudes in the frequency bands outside the attenuation zone (for example, 6–10 Hz) that makes it difficult to achieve attenuation.

Time history analyses were performed by applying seismic inputs directly to the source location. For the FE models with or without graded metasurfaces, the average acceleration responses in the vertical direction were calculated in the detection area. After the acquisition, fast Fourier transform was applied to the output responses, and their frequency components were compared to highlight the attenuation effect in the decreasing-frequency case. Figure 16 displays the normalized average vertical acceleration responses and corresponding Fourier spectra at the output area, considering the presence or absence of graded metasurfaces. It can be found that the vertical acceleration amplitude in the FE model with graded metasurfaces (denoted as solid red lines) is reduced by 39%, 27%, and 25%, respectively, compared with those in the reference model (denoted as solid blue lines). Simultaneously, the

corresponding frequency components at Output 1 (graded metasurface), as shown in Figure 16(b), (d), and (f) are significantly reduced in the attenuation zone compared with those at Output 2 (free surface). In conclusion, the above results once again prove that the tuned resonant metasurfaces can achieve broadband surface wave attenuation and are expected to effectively avoid seismic damage to critical infrastructures.

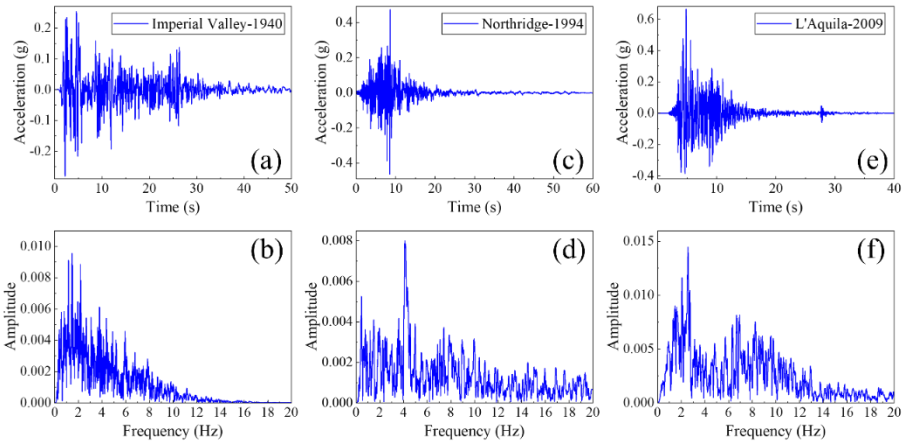

Figure 15. Input seismic wave acceleration records and corresponding Fourier spectra. (a, b) Imperial Valley earthquake; (c, d) Northridge earthquake and (e, f) L'Aquila earthquake.[52]

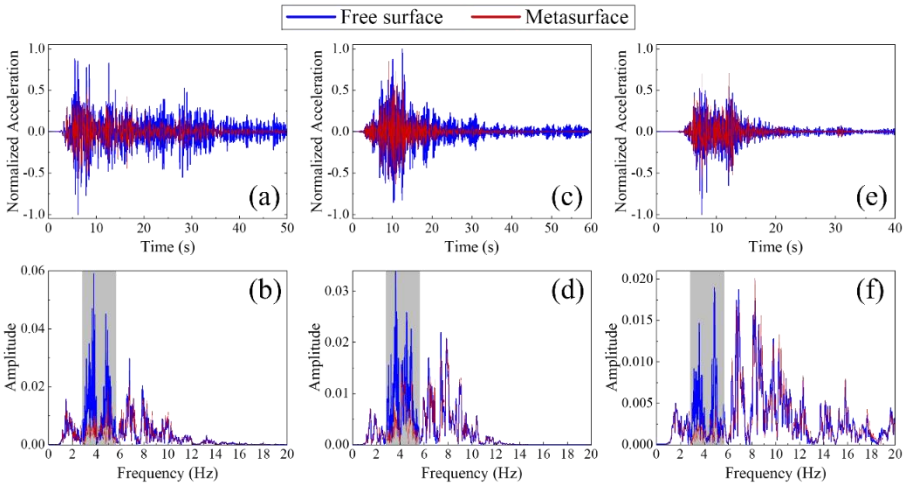

Figure 16. Normalized average vertical acceleration response at the output area and corresponding Fourier spectra with and without metasurfaces. (a, b) Imperial Valley earthquake; (c, d) Northridge earthquake; and (e, f) L'Aquila earthquake.

5 CONCLUSIONS

The recent proliferation of resonant metamaterials developed for seismic wave shielding is based on stimulated theoretical and analytical frameworks capable of describing the interaction of surface waves with longitudinal resonance metasurfaces. Within this context, this study theoretically investigates the dispersion properties in the

actual site conditions by considering the coupling of Rayleigh waves with metasurfaces attached to the free surface of a stratified semi-infinite space. The dispersion curves of the three configurations, including a stratified soil system, a homogeneous soil–resonator coupling system, and a stratified soil–resonator coupling system, were obtained by numerical simulations. Additionally, a finite-length metasurface and a graded resonant metasurface with decreasing frequency were used to evaluate the attenuation efficiency in the frequency domain and time domain, respectively. The main findings of this study are summarized as follows:

(1) The analytical framework is developed by introducing the classical elastodynamics theory and an effective medium description to investigate the eigen equation of Raleigh waves propagating through periodically distributed vertical resonators in multiple stratified soil substrates. Simultaneously, the improved matrix algorithm proposed in this study can be used to calculate the dispersion relations of stratified soil–resonator interactions promptly and accurately, avoiding the problem of high-frequency effective digit loss.

(2) The analytical and numerical solutions of the dispersion curves are in good agreement that validates the feasibility of the Bloch-wave FE method. It is observed that the first-order surface mode gradually becomes a flat dispersive branch near the metasurface resonance, while the other higher-order surface modes still cross the surface wave band gap. Thus, it is highlighted that only the first-order mode is strongly coupled with the resonant metasurfaces, and the effect of the higher-order modes is negligible.

(3) The results of harmonic analyses show that the transmission model with a finite-length metasurface exhibits a sharp attenuation in a narrow frequency range near resonance. In addition, the coupling degree of Rayleigh waves and hybrid Rayleigh waves at the soil–resonator interface is sensitive to the resonator mass m_0. Broadband attenuation can be achieved by increasing the resonator mass or metasurface length within a certain range.

(4) By reasonably adjusting the resonator mass or spring compression stiffness, it is possible to obtain a graded metasurface with an ultra-low starting frequency and broadband attenuation. In particular, it is found that the vertical acceleration amplitude in the output region of the FE model with a graded resonant metasurface can be reduced by 39% relative to the reference model.

As mentioned above, the actual site conditions are far more complex than the stratified case assumed in this paper; for example, weak interbeds and groundwater are common in practice. Moreover, the failure of soil bearing capacity caused by the large resonating masses should be checked according to real site conditions. Further research efforts will be devoted to develop 3D resonant metasurfaces and investigate the resonators damping, soil nonlinearity, and activation time of the resonant metasurfaces on the shielding effect. One can expect a substantial volume of quantitative studies on seismic metabarriers using realistic materials and structural paremeters in the coming years.

REFERENCES

1. Hussein MI, Leamy MJ, Ruzzene M. Dynamics of Phononic Materials and Structures: Historical Origins, Recent Progress, and Future Outlook. *Appl Mec Rev* 2014;66(4):040802.
2. Yablonovitch E. Inhibited Spontaneous Emission in Solid-State Physics and Electronics. *Phys Rev Lett* 1987;58(20):2059–2062.

3. John S. Strong localization of photons in certain disordered dielectric superlattices. *Phys Rev Lett* 1987;58(23):2486–2489.
4. Kushwaha MS, Halevi P, Dobrzynski L, Djafari-Rouhani B. Acoustic band structure of periodic elastic composites. *Phys Rev Let* 1993;71(13):2022–2025.
5. Liu Z. Locally Resonant Sonic Materials. *Science* 2000;289(5485):1734–1736.
6. Zhang X, Liu Z. Negative refraction of acoustic waves in two-dimensional phononic crystals. *Appl Phys Lett* 2004;85(2):341–343.
7. Sukhovich A, Jing L, Page JH. Negative refraction and focusing of ultrasound in two-dimensional phononic crystals. *Phys Rev B* 2008;77(1):014301.
8. Kan W, Shen Z. Ultra-transparent media with anisotropic mass density for broadband acoustic invisibility. *Appl Phys Lett* 2017;111(22):223501.
9. Zhu J, Chen T, Song X, Chen C, Liu Z, Zhang J. Three-dimensional large-scale acoustic invisibility cloak with layered metamaterials for underwater operation. *Phys Scripta* 2019;94(11):115003.
10. Sukhovich A, Merheb B, Muralidharan K, Vasseur JO, Pennec Y, Deymier PA, et al. Experimental and Theoretical Evidence for Subwavelength Imaging in Phononic Crystals. *Phys Rev Lett* 2009;102(15):154301.
11. Bak AO, Giannini V, Maier SA, Phillips CC. Super-resolution with a positive epsilon multi-quantum-well super-lens. *Appl Phys Lett* 2013;103(26):261110.
12. Tsung-Tsong Wu, Jin-Chen Hsu, Jia-Hong Sun. Phononic plate waves. *IEEE T Ultrason Ferr* 2011;58(10):2146–2161.
13. Thota M, Wang KW. Tunable waveguiding in origami phononic structures. *J Sound Vib* 2018;430(1):93–100.
14. Muzar E, Aval GA, Stotz JAH. Wet-etched phononic crystal waveguiding on GaAs. *J Phys D Appl Phys* 2018;51(4):044001.
15. Chen H, Chan CT. Acoustic cloaking and transformation acoustics. *J Phys D Appl Phys* 2010;43(11):113001.
16. Brun M, Guenneau S, Movchan AB. Achieving control of in-plane elastic waves. *Appl Phys Lett* 2009;94(6):061903.
17. Chen H, Chan CT. Acoustic cloaking in three dimensions using acoustic metamaterials. *Appl Phys Lett* 2007;91(18):183518.
18. Chen YY, Barnhart MV, Chen JK, Hu GK, Sun CT, Huang GL. Dissipative elastic metamaterials for broadband wave mitigation at subwavelength scale. *Compos Struct* 2016;136:358–371.
19. Gonella S, To AC, Liu WK. Interplay between phononic bandgaps and piezoelectric microstructures for energy harvesting. *J Mech Phys Solids* 2009;57(3):621–633.
20. Miniaci M, Krushynska A, Bosia F, Pugno NM. Large scale mechanical metamaterials as seismic shields. *New J Phys* 2016;18(8):083041.
21. Basone F, Wenzel M, Bursi OS, Fossetti M. Finite locally resonant Metafoundations for the seismic protection of fuel storage tanks. *Earthq Eng Struct D* 2019;48(2):232–252.
22. Brûlé S, Javelaud EH, Enoch S, Guenneau S. Experiments on Seismic Metamaterials: Molding Surface Waves. *Phys Rev Lett* 2014;112(13):133901.
23. Zhao C, Zeng C, Huang H, Dai J, Bai W, Wang J, et al. Preliminary study on the periodic base isolation effectiveness and experimental validation. *Eng Struct* 2021;226(7):111364.
24. Zhao C, Zeng C, Witarto W, wen Huang H, Dai J, Mo YL. Isolation performance of a small modular reactor using 1D periodic foundation. *Eng Struct* 2021;244(9–10):112825.

25. Leonhardt U. Optical Conformal Mapping. *Science* 2006;312(5781):1777–1780.
26. Pendry JB. Controlling Electromagnetic Fields. *Science* 2006;312(5781):1780–1782.
27. Yu JK, Mitrovic S, Tham D, Varghese J, Heath JR. Reduction of thermal conductivity in phononic nanomesh structures. *Nat Nanotechnol* 2010;5(10):718–721.
28. Cheng ZB, Shi ZF. Composite periodic foundation and its application for seismic isolation. *Earthq Eng Struct D* 2018;47(4):925–944.
29. Xiang HJ, Shi ZF, Wang SJ, Mo YL. Periodic materials-based vibration attenuation in layered foundations: experimental validation. *Smart Mater Struct* 2012;21(11):112003.
30. Colombi A, Roux P, Guenneau S, Gueguen P, Craster RV. Forests as a natural seismic metamaterial: Rayleigh wave bandgaps induced by local resonances. *Sci Rep* 2016;6(1):19238.
31. Colombi A, Colquitt D, Roux P, Guenneau S, Craster RV. A seismic metamaterial: The resonant metawedge. *Sci Rep* 2016;6(1):27717.
32. Colquitt DJ, Colombi A, Craster RV, Roux P, Guenneau SRL. Seismic metasurfaces: Sub-wavelength resonators and Rayleigh wave interaction. *J Mech Phys Solids* 2017;99:379–393.
33. Palermo A, Krödel S, Marzani A, Daraio C. Engineered metabarrier as shield from seismic surface waves. *Sci Rep* 2016;6(1):39356.
34. Liu C heng, Nagel SR. Sound in sand. *Phys Rev Lett* 1992;68(15):2301–2304.
35. Palermo A, Krödel S, Matlack KH, Zaccherini R, Dertimanis VK, Chatzi EN, et al. Hybridization of Guided Surface Acoustic Modes in Unconsolidated Granular Media by a Resonant Metasurface. *Phys Rev Appl* 2018;9(5):054026.
36. Zaccherini R, Palermo A, Marzani A, Colombi A, Dertimanis V, Chatzi E. Mitigation of Rayleigh-like waves in granular media via multi-layer resonant metabarriers. *Appl Phys Lett* 2020;117(25):254103.
37. Zeighami F, Palermo A, Vratsikidis A, Cheng Z, Pitilakis D, Marzani A. Medium-scale resonant wave barrier for seismic surface waves. *Mech Based Des Struc* 2020:1–16.
38. Pu X, Palermo A, Cheng Z, Shi Z, Marzani A. Seismic metasurfaces on porous layered media: Surface resonators and fluid-solid interaction effects on the propagation of Rayleigh waves. *Int J Eng Sci* 2020;154:103347.
39. Graff KF. *Wave motion in elastic solids*. Revised edition. New York: Dover Publications; 1991.
40. Kushwaha MS, Halevi P, Martínez G, Dobrzynski L, Djafari-Rouhani B. Theory of acoustic band structure of periodic elastic composites. *Phys Rev B* 1994;49(4):2313–2322.
41. Knopoff L. A matrix method for elastic wave problems. *B Seismol Soc Am* 1964;54(1):431–438.
42. Dunkin JW. Computation of modal solutions in layered, elastic media at high frequencies. *B Seismol Soc Am* 1965;55(2):335–358.
43. Thrower EN. The computation of the dispersion of elastic waves in layered media. *J Sound Vib* 1965;2(3):210–226.
44. Abo-Zena A. Dispersion function computations for unlimited frequency values. *Geophys J Int* 1979;58(1):91–105.
45. Cai C, Gao L, He X, Zou Y, Yu K, Wu D. The surface wave attenuation zone of periodic composite in-filled trenches and its isolation performance in train-induced ground vibration isolation. *Comput Geotech* 2021;139:104421.
46. Palermo A, Vitali M, Marzani A. Metabarriers with multi-mass locally resonating units for broad band Rayleigh

waves attenuation. *Soil Dyn Earthq Eng* 2018;113:265–277.
47. Moser F, Jacobs LJ, Qu J. Modeling elastic wave propagation in waveguides with the finite element method. *Ndt&e Int* 1999;32(4):225–234.
48. De Marchi L, Marzani A, Miniaci M. A dispersion compensation procedure to extend pulse-echo defects location to irregular waveguides. *Ndt&e Int* 2013;54:115–122.
49. Phani AS, Woodhouse J, Fleck NA. Wave propagation in two-dimensional periodic lattices. *J Acoust Soc Am* 2006;119(4):1995–2005.
50. Huang J, Liu W, Shi Z. Surface-wave attenuation zone of layered periodic structures and feasible application in ground vibration reduction. *Constr Build Mater* 2017;141:1–11.
51. Boechler N, Eliason JK, Kumar A, Maznev AA, Nelson KA, Fang N. Interaction of a Contact Resonance of Microspheres with Surface Acoustic Waves. *Physl Rev Lett* 2013;111(3):036103.
52. Pacific Earthquake Engineering Research Center. https://ngawest2.berkeley.edu/

APPENDIX: Definition of the matrix elements

The matrix **H** is:

$$\mathbf{H}=\begin{bmatrix} 1 & 1 & \gamma_S & \gamma_S \\ \gamma_L & -\gamma_L & 1 & -1 \\ \rho(\gamma-1) & \rho(\gamma-1) & \rho\gamma\gamma_S & \rho\gamma\gamma_S \\ \rho\gamma\gamma_L & -\rho\gamma\gamma_L & \rho(\gamma-1) & -\rho(\gamma-1) \end{bmatrix}. \tag{A1}$$

The matrix $\mathbf{H}^{-1}$ is

$$\mathbf{H}^{-1}=\frac{1}{2}\begin{bmatrix} \gamma & -\frac{\gamma-1}{\gamma_L} & -\frac{1}{\rho} & \frac{1}{\rho\gamma_L} \\ \gamma & \frac{\gamma-1}{\gamma_L} & -\frac{1}{\rho} & -\frac{1}{\rho\gamma_L} \\ -\frac{\gamma-1}{\gamma_S} & \gamma & \frac{1}{\rho\gamma_S} & -\frac{1}{\rho} \\ -\frac{\gamma-1}{\gamma_S} & -\gamma & \frac{1}{\rho\gamma_S} & \frac{1}{\rho} \end{bmatrix}. \tag{A2}$$

The matrix $\mathbf{E}_m^*$ is:

$$\mathbf{E}_m^* = diag\begin{bmatrix} 1 & PQ & \frac{P}{Q} & \frac{Q}{P} & \frac{1}{PQ} & 1 \end{bmatrix}. \tag{A3}$$

The elements of matrix $\mathbf{H}_m^*$ are:

$$\begin{aligned} h_{11}^* &= -2\gamma_L & h_{12}^* &= 1-\gamma_L\gamma_S & h_{13}^* &= -1-\gamma_L\gamma_S \\ h_{14}^* &= 1+\gamma_L\gamma_S & h_{15}^* &= -1+\gamma_L\gamma_S & h_{16}^* &= -2\gamma_S \end{aligned} \tag{A4}$$

$h_{21}^{*}=0$ $h_{22}^{*}=\rho\gamma_S$ $h_{23}^{*}=\rho\gamma_S$

$h_{24}^{*}=\rho\gamma_S$ $h_{25}^{*}=\rho\gamma_S$ $h_{26}^{*}=0$

$h_{31}^{*}=-2\rho\gamma\gamma_L$ $h_{32}^{*}=\rho(\gamma-1)-\rho\gamma\gamma_L\gamma_S$ $h_{33}^{*}=-\rho(\gamma-1)-\rho\gamma\gamma_L\gamma_S$

$h_{34}^{*}=\rho(\gamma-1)+\rho\gamma\gamma_L\gamma_S$ $h_{35}^{*}=-\rho(\gamma-1)+\rho\gamma\gamma_L\gamma_S$ $h_{36}^{*}=-2\rho\gamma_S(\gamma-1)$

$h_{41}^{*}=2\rho\gamma_L(\gamma-1)$ $h_{42}^{*}=\rho\gamma\gamma_L\gamma_S-\rho(\gamma-1)$ $h_{43}^{*}=\rho\gamma\gamma_L\gamma_S+\rho(\gamma-1)$

$h_{44}^{*}=-\rho\gamma\gamma_L\gamma_S-\rho(\gamma-1)$ $h_{45}^{*}=-\rho\gamma\gamma_L\gamma_S+\rho(\gamma-1)$ $h_{46}^{*}=2\rho\gamma\gamma_S$

$h_{51}^{*}=0$ $h_{52}^{*}=-\rho\gamma_L$ $h_{53}^{*}=\rho\gamma_L$

$h_{54}^{*}=\rho\gamma_L$ $h_{55}^{*}=-\rho\gamma_L$ $h_{56}^{*}=0$

$h_{61}^{*}=-2\rho^2\gamma\gamma_L(\gamma-1)$ $h_{62}^{*}=\rho^2(\gamma-1)^2-(\rho\gamma)^2\gamma_L\gamma_s$ $h_{63}^{*}=-\rho^2(\gamma-1)^2-(\rho\gamma)^2\gamma_L\gamma_s$

$h_{64}^{*}=\rho^2(\gamma-1)^2+(\rho\gamma)^2\gamma_L\gamma_s$ $h_{65}^{*}=-\rho^2(\gamma-1)^2+(\rho\gamma)^2\gamma_L\gamma_s$ $h_{66}^{*}=-2\rho^2\gamma\gamma_s(\gamma-1)$

764

765 The elements of matrix $(\mathbf{H}_m^{-1})^{*}$ are:

$H_{11}^{*}=-\frac{2\gamma(\gamma-1)}{\gamma_L}$ $H_{12}^{*}=0$ $H_{13}^{*}=-\frac{2\gamma}{\rho\gamma_L}$ $H_{14}^{*}=\frac{2(\gamma-1)}{\rho\gamma_L}$

$H_{15}^{*}=0$ $H_{16}^{*}=\frac{2}{\rho^2\gamma_L}$ $H_{21}^{*}=\gamma^2-\frac{(\gamma-1)^2}{\gamma_L\gamma_S}$ $H_{22}^{*}=\frac{1}{\rho\gamma_S}$

$H_{23}^{*}=-\frac{\gamma}{\rho}+\frac{\gamma-1}{\rho\gamma_L\gamma_S}$ $H_{24}^{*}=\frac{\gamma}{\rho}-\frac{\gamma-1}{\rho\gamma_L\gamma_S}$ $H_{25}^{*}=-\frac{1}{\rho\gamma_L}$ $H_{26}^{*}=\frac{1}{\rho^2}-\frac{1}{\rho^2\gamma_L\gamma_S}$

$H_{31}^{*}=-\gamma^2-\frac{(\gamma-1)^2}{\gamma_S\gamma_L}$ $H_{32}^{*}=\frac{1}{\rho\gamma_S}$ $H_{33}^{*}=\frac{\gamma}{\rho}+\frac{\gamma-1}{\rho\gamma_L\gamma_S}$ $H_{34}^{*}=-\frac{\gamma}{\rho}-\frac{\gamma-1}{\rho\gamma_L\gamma_S}$

$H_{35}^{*}=\frac{1}{\rho\gamma_L}$ $H_{36}^{*}=-\frac{1}{\rho^2}-\frac{1}{\rho^2\gamma_L\gamma_S}$ $H_{41}^{*}=\gamma^2+\frac{(\gamma-1)^2}{\gamma_L\gamma_S}$ $H_{42}^{*}=\frac{1}{\rho\gamma_S}$ (A5)

$H_{43}^{*}=-\frac{\gamma}{\rho}-\frac{\gamma-1}{\rho\gamma_L\gamma_S}$ $H_{44}^{*}=\frac{\gamma}{\rho}+\frac{\gamma-1}{\rho\gamma_L\gamma_S}$ $H_{45}^{*}=\frac{1}{\rho\gamma_L}$ $H_{46}^{*}=\frac{1}{\rho^2}+\frac{1}{\rho^2\gamma_L\gamma_S}$

$H_{51}^{*}=-\gamma^2+\frac{(\gamma-1)^2}{\gamma_L\gamma_S}$ $H_{52}^{*}=\frac{1}{\rho\gamma_S}$ $H_{53}^{*}=\frac{\gamma}{\rho}-\frac{\gamma-1}{\rho\gamma_L\gamma_S}$ $H_{54}^{*}=-\frac{\gamma}{\rho}+\frac{\gamma-1}{\rho\gamma_L\gamma_S}$

$H_{55}^{*}=-\frac{1}{\rho\gamma_L}$ $H_{56}^{*}=-\frac{1}{\rho^2}+\frac{1}{\rho^2\gamma_L\gamma_S}$ $H_{61}^{*}=\frac{2\gamma(\gamma-1)}{\gamma_S}$ $H_{62}^{*}=0$

$H_{63}^{*}=-\frac{2(\gamma-1)}{\rho\gamma_S}$ $H_{64}^{*}=\frac{2\gamma}{\rho\gamma_S}$ $H_{65}^{*}=0$ $H_{66}^{*}=\frac{2}{\rho^2\gamma_S}$

766